Correlating 3D porous structure in polymer films with mass transport properties using FIB-SEM tomography

Chemical Engineering Science: X xxx (xxxx) xxx

Contents lists available at ScienceDirect

Chemical Engineering Science: X

journal homepage: www.elsevier.com/locate/cesx

Correlating 3D porous structure in polymer films with mass transport properties using FIB-SEM tomography

C. Fager [a,*], T. Gebäck [b], J. Hjärtstam [c], M. Röding [b,d], A. Olsson [c], N. Lorén [a,d], C. von Corswant [c], A. Särkkä [b], E. Olsson [a]

[a] Department of Physics, Chalmers University of Technology, SE-41296 Gothenburg, Sweden
[b] Department of Mathematical Sciences, Chalmers University of Technology and University of Gothenburg, Gothenburg, Sweden
[c] AstraZeneca R&D Mölndal, SE43183 Mölndal, Sweden
[d] RISE Research Institutes of Sweden, Agriculture and Food, Gothenburg, Sweden

ARTICLE INFO

Article history:
Received 27 November 2020
Received in revised form 5 July 2021
Accepted 14 July 2021
Available online xxxx

Keywords:
Focused ion beam
Mass transport
Scanning electron microscopy
Polymer
Soft material
Three dimensional

ABSTRACT

Porous polymer coatings are used to control drug release from pharmaceutical products. The coating covers a drug core and depending on the porous structure, different drug release rates are obtained. This work presents mass transport simulations performed on porous ethyl cellulose films with different porosities. The simulations were performed on high spatial resolution 3D data obtained using a focused ion beam scanning electron microscope. The effective diffusion coefficient of water was determined using a diffusion chamber. Lattice Boltzmann simulations were used to simulate water diffusion in the 3D data. The simulated coefficient was in good agreement with the measured coefficient. From the results it was concluded that the tortuosity and constrictivity of the porous network increase with decreasing amount of added hydroxypropyl cellulose, resulting in a sharp decrease in effective diffusion. This work shows that high spatial resolution 3D data is necessary, and that 2D data is insufficient, in order to predict diffusion through the porous structure with high accuracy.

Introduction

During the last decades, there has been growing interest in porous structures in materials and the optimisation of their properties. The function of the porous structure can vary depending on its application. It is well-known that the 3D structure strongly influences transport properties. For example, the porous structures in solar cells, fuel cells and batteries play a very important role in electric and ionic conductivity (Stenzel et al., 2016; Holzer et al., 2013). The porous structure influences the transport properties also in biological materials such as tissue engineering scaffolds used for bone ingrowth (Jones et al., 2009). Furthermore, the porous structure is critical in polymer coatings used for controlled drug release (Siepmann et al., 2007). Here, we study coatings that consist of two immiscible polymers, one polymer that is water insoluble and one that is not. The water soluble polymer is leached out upon contact with water in the body, leaving the water insoluble polymer with an internal porous structure. The porous structure acts as a transport path for the drug and thus can be used to tailor the drug release through the porous polymer coating. It is, therefore, important to study the correlation between the 3D porous structure and the transport properties of the coating. Previous research has shown that pore connectivity strongly influences transport properties (Armatas, 2006; Vogel, 1997; Ghassemzadeh and Sahimi, 2004; Yang et al., 2014). Interconnectivity describes the extent to which the pores are connected and can be quantified by calculating the shortest possible path that starts at an inlet pore, ends at an outlet pore, and passes through a specific point in the structure (Fager et al., 2020). Such pore paths are called geodesic paths. In the case of low porosity, it has been shown that many paths coincide into a channel. The degree of the importance of a channel for the transport can be measured using a channel strength measurement (Fager et al., 2020). A high channel strength indicates that many paths have coincided and the overall interconnectivity is low, indicating reduced diffusive transport rate.

There are several different approaches and advanced techniques available to study transport properties in porous materials. For example, terahertz pulsed imaging has been used to characterise and study the disintegration of highly porous tablets experimentally (Markl et al., 2018). It can provide the high acquisition rate needed in the analysis of the fast water transport, i.e. the liquid imbibition of water into the tablets. The terahertz data showed

* Corresponding author.
E-mail address: cecilia.fager@outlook.com (C. Fager).

https://doi.org/10.1016/j.cesx.2021.100109
2590-1400/

fluctuations of the liquid movement which became more pronounced and higher in frequency with increasing porosity showing that the structure of the tablet strongly influences the transport properties of the tablet.

Furthermore, the interaction of controlled-release polymer coatings with water has been studied *in situ* in an environmental scanning electron microscope, enabling direct visual observation of the water transport through the coating film as well as the swelling and dissolution of the water-soluble polymer, at a high spatial resolution (Jansson et al., 2014)

There are several well-established 3D imaging techniques and which one to use depends e.g. on the type of material and the required resolution. If the aim is to image structures at a larger length scale, from millimeter to micrometer scale, then optical microscopes are preferred while electron microscopes are preferred at smaller length scales down to nanometer scale (Narayan and Subramaniam, 2015). For example, confocal laser scanning microscopy (CLSM) can be used to produce 3D data in micrometer length scale (Gebäck et al., 2015). Therefore, it is a suitable method for relatively large volumes of materials that are optically transparent and have minor differences in the refractive index in the material. CLSM can be combined with mass transport simulations (Wassén et al., 2014). However, in confocal microscopy the resolution becomes worse in the depth direction of the specimen. To obtain 3D data at the smaller, e.g. nanometer, length scale, transmission electron microscopy (TEM) tomography can be used. In combination with mass transport simulations, it is a truly powerful tool for increasing the understanding of mass transport through porous structures on the micro and nano scale (Blomqvist, 2016). However, it is limited to very small volumes due to the thin TEM specimen.

Combination imaging with mass transport simulations provides a means to investigate how the microstructural features of a material can be used to control the transport of fluids and molecules through it. Although simplified relationships have been found and used for decades to compute mass transport coefficients, such as effective diffusion constants and fluid permeability, they do not provide a detailed understanding of the correlation between the material structure and its mass transport properties. However, by performing simulations in real 3D structures, and structures modified *in silico*, a more detailed understanding of this correlation can be obtained (Röding et al., 2016). This in turn can be used for design of novel materials with optimised transport properties. Several methods may be used for computation of mass transport properties. Here, we use the lattice Boltzmann method (Krüger et al., 2017; Gebäck and Heintz, 2014) which has extensively been used for simulations in porous media since it is relatively easy to use parallel computing enabling computations in large domains and relative simply to implement boundary conditions in complex geometries. Other methods, such as finite element methods or finite volume methods, can also be used, but they require some meshing steps and are less suitable for parallel computations.

In this work, real 3D structures of polymer films, made of a phase-separated blend of ethyl cellulose and hydroxypropyl cellulose, used for controlled drug release have been linked to the transport properties of the material. The polymer films are made from a phase-separated blend of ethyl cellulose and hydroxypropyl cellulose, where only the latter is water soluble. It is crucial to understand the link between the 3D structures and the transport properties in order to design the structure so that a tailored drug release can be achieved. We acquired high spatial resolution 3D data using FIB-SEM tomography and determined the effective diffusion coefficient both by simulations and by experiments. Three films with different porosities were investigated. The films were leached in water whereby the porous structure in ethyl cellulose was formed through the removal of the water-soluble hydroxypropyl cellulose. The results show a more evenly distributed mass transport through the films as the porosity increases. The simulated and experimentally measured effective diffusion coefficients were in good agreement with each other. This work shows that high spatial resolution 3D data on porous polymers combined with mass transport simulations can be used to accurately predict diffusion in porous media.

Experimental and theoretical methods

Preparation of porous polymer films

Porous polymer films used for controlled drug release, consisting of one water soluble polymer and one water insoluble polymer, were prepared as described in Marucci et al. (Marucci et al., 2009). In short, ethyl cellulose (EC) (Ethocel™ Standard 10 from Dow Wolff Cellulosic GmbH in Germany) and hydroxypropyl cellulose (HPC) (Klucel® LF from Ashland in USA) were dissolved in ethanol (95%) and stirred on a magnetic plate for 24 h to obtain a homogenous solution. The dry weight of the solution was 6%. The free film was prepared by spraying an even layer of the polymer solution on a rotating heated Teflon drum. After drying for about 20 min the film was carefully removed from the drum. Three different films with 22, 30, and 45 wt-% HPC denoted by HPC22, HPC30 and HPC45, respectively, were produced. The films were then leached in deionised water for 24 hrs to remove the HPC phase resulting in a porous EC phase structure. The porous polymer films were air dried and mounted onto an aluminum stub with adhesive carbon tape. Finally, the films were coated with a few nanometers of palladium using a sputtering device, Emitech K550X (Quorum Technologies Ltd, Ashford, United Kingdom), to reduce charging in the focused ion beam scanning electron microscope.

Focused ion beam scanning electron microscopy tomography

The 3D structure of the porous polymer films was imaged using a focused ion beam scanning electron microscope (FIB-SEM) from Tescan Gaia3 (Czech Republic). The ion beam was used to remove 50 nm thin slices, and the electron beam to image each resulting cross section (Giannuzzi and Stevie, 2005). The ion beam parameters used for this study were 30 kV and 1nA and the electron beam parameters were below 700 V and below 10 pA. A platinum layer of a few micrometers thickness was deposited on the specimen surface to prevent charging and to protect the surface underneath from being damaged by the ion beam (Mayer et al., 2007). The detailed information about the protocol for optimising the parameters of the ion beam and the electron beam for soft porous materials are described in detail in (Fager et al., 2020).

3D reconstruction

The 200 sequential 2D images obtained using FIB-SEM tomography were aligned and cropped using the software ImageJ with the StackReg plugin and the Rigid Body method (Schneider et al., 2012). The imaged region was $30 \times 20 \times 10$ μm, with a resolution of 10 nm in the cross (x, y) directions and 50 nm in the slicing (z) direction. The 3D reconstruction of the material requires segmentation of the solid and pore phases in each image of the 2D stack. A machine learning approach developed using Matlab (Mathworks) was used for segmentation. The method was described in detail in (Röding et al., 2021) and briefly recapitulated here. First, manual segmentation was performed by an expert on a subset of the full data, consisting of 100 randomly placed square regions of 256×256 pixels per data set. Second, 2D Gaussian filters with standard deviations sigma = 1, 2, 4, 8, 16, 32, 64, and

128 pixels were applied to the slice to be segmented and to five adjacent slices in each direction, and also the original data (corresponding to sigma = 0) was used. In total, this yields 99 features. Third, a random forest classifier was trained on these data to classify individual pixels as either solid or pore. Fourth, the method was applied to the full data sets after training and testing on the manually segmented subset of the data. For diffusion simulations, the segmented images were sub-sampled such that every fifth voxel was taken in the x- and y-direction, resulting in an isotropic voxel size of 50 nm in all directions.

Permeability measurements

The permeation experiment was performed using a diffusion chamber consisting of two chambers separated by the film to be investigated, see e.g. (Gårdebjer et al., 2018). A circular film segment was cut out of the cast film, and the thickness was measured with a micrometer screw gauge. A piece of the film was then placed between the two cell compartments. At the beginning of each experiment, 15 mL of deionised water was added to both cell compartments simultaneously, to avoid any pressure on the membrane. After 15 min, a small amount of tritiated water (10 μl, 400 kBq) was added to the donor compartment and two paddles were used to stir the water at a speed of 200 rpm. A water jacket containing 37 °C water maintained the temperature throughout the experiment. Samples of 500 μl were taken from the receiver compartment at specified time intervals and replaced by the same amount of pure distilled water. 4 mL of scintillation liquid was added to each sample. The samples were then placed in a Wallac Win Spectral model 1414 liquid scintillator counter. The increase in tritium activity in the receiver compartment was divided by the tritium activity per unit volume in the donor cell and finally the permeability of the film could be calculated (Lindstedt et al., 1989). As the tritium activity in the donor compartment is much higher than in the receiver, the counter-diffusion of tritium was neglected.

Diffusion simulations

4. In order to compute the effective diffusion constant of the structures, the lattice Boltzmann method (Gebäck and Heintz, 2014; Ginzburg, 2005) was employed to solve the diffusion equation (1)

$$\frac{\partial c}{\partial t} - D_0 \Delta c = 0 \tag{1}$$

numerically for the solute concentration c in the pores. Here, D_0 is the free diffusion coefficient of the solute in the pore space and we used the value $D_0 = 2.96 \cdot 10^{-9}$ m^2/s for tritiated water at 37 °C (Mills, 1973). On the material surface, Neumann (zero normal flux) boundary conditions

$$\frac{\partial c}{\partial n} = 0, \tag{2}$$

where n is the outward unit normal, were used to model that no diffusion takes place in the solid EC phase. The details of the method, in particular the implementation of the boundary conditions, are described in (Gebäck and Heintz, 2014). At the top and bottom of the sample, at $y = 0$ and $y = L$, the concentration was set to constant values (c_1 and c_2, respectively) to create a concentration gradient across the sample. The Neumann boundary condition (2) was also used on the other boundaries of the simulation box to model the effect of a continuous material structure with mirror symmetry across the boundary. The diffusion equation was solved to steady state, and the effective diffusion coefficient was then computed as $D_{eff} = -\bar{J}_y L/(c_2 - c_1)$ from the average flux $\bar{J}_y = \langle -D_0 \partial c/\partial y \rangle$ in the direction of the concentration gradient, were the average is taken over the whole volume, not only the pore space.

The segmented data for the HPC30 and HPC45 samples were downsampled to a grid size of 600 × 400 × 200 voxels with a voxel size of 50 nm in all directions. The simulations were run in parallel on 60 cores. For the HPC22 sample, this resolution was insufficient to resolve all the narrow pores in the sample and the data were, therefore, resampled to a grid of 900 × 600 × 300 voxels with a voxel size of 33 nm. However, even at this resolution there was just barely a connected path through the whole structure with a connection through very narrow pores. Therefore, the sample was divided into five overlapping regions in the y-direction, each of thickness 200 voxels. For each of these regions several connected paths were present through the whole region. Simulations yielded the respective effective diffusion coefficients $D_1, \cdots, D_5$. The total effective diffusion coefficient was then computed as

$$\frac{Nl}{D_{eff}} = \sum_{k=1}^{N} \frac{l}{2}\left(\frac{1}{D_{k-1}} + \frac{1}{D_k}\right) \tag{3}$$

with $N = 6$ and $l = 100$, where we set $D_0 = D_1$ and $D_6 = D_5$. This corresponds to dividing the sample into six non-overlapping regions of thickness $l = 100$ voxels and placing them in series, using for each region the hyperbolic average of the diffusion coefficients for the computational domains that overlap with it. This way, the result for the HPC22 sample is not dependent on resolving the connected paths through the entire sample, which in our case led to an unfeasible computational effort. However, the result obtained may well be more representative of the whole material as it is less dependent on the particularities of the imaged region. The other two samples were also similarly divided into overlapping slices of thickness 6.67 μm and the local effective diffusion coefficients and porosities were computed for investigation of the local behaviour.

Structural properties

In order to explain the diffusion results for the films, we also computed the geodesic tortuosity τ, according to Barman et al (Barman et al., 2018). This value is computed by computing the shortest path to inlet and outlet from each pore voxel to compute the local tortuosity, and then averaging the inverse squares of the local tortuosities to compute $1/\tau^2$, and then τ. The geodesic tortuosity quantifies the length of paths through the structure, which has a strong influence on the effective diffusion coefficient.

Additionally, the constriction factor β is computed according to the definition by Holzer et al (Barman et al., 2019) as

$$\beta = \frac{A_{min}}{A_{max}} = \frac{\pi r_{min}^2}{\pi r_{max}^2} \tag{4}$$

where A_{min} and A_{max} are minimum and maximum cross-sectional areas of pores, which are assumed to be circular with effective radii r_{min} and r_{max}, respectively. The minimal radius r_{min} is estimated as the median radius from a virtual mercury intrusion porosimetry, while the maximal radius r_{max} is computed as the median radius from a regular pore size distribution. The constriction factor quantifies the effect on diffusion of varying pore sizes along pores.

Both τ and β were computed using the software Mist (Barman et al., 2019), version 1.0.6, and more computational details can be found in the documentation of the software.

Results and discussion

High spatial resolution 3D data of porous polymer films with different porosities and their corresponding 3D diffusion simula-

tions can be seen in Fig. 1. The 3D data were obtained using a FIB-SEM. The contrast in Fig. 1 a, c, e corresponds to the different features of the porous network. The darker regions belong to deeper pores, the regions of intermediate intensity belong to the solid ethyl cellulose (EC) and the brighter regions belong to shallow pores. For the case of HPC30, some overexposed areas can be seen, and these areas belong to the EC solid. Segmentation of these different intensities was performed using a machine-learning segmentation algorithm (Röding et al., 2021). The three porous polymer films in Fig. 1a) HPC22, 1c) HPC30 and 1e) HPC45 differ in the total porosity. In a recent paper, the total pore volume and median pore diameter for the three films were calculated to 20% and 0.35 μm for HPC22, 30 % and 0.60 μm for HPC30, and finally, 44 % and 0.72 μm for HPC45 (Röding et al., 2021).

The simulated diffusion through the porous polymer films with different porosities is shown in Fig. 1 b, d, f. One single line inlet on the upper film surface has been selected to visualise the flux lines from top to bottom. The colour of the flux lines represents the magnitude of the flux. The blue colour corresponds to low flux while red colour corresponds to higher flux. Bottlenecks, i.e. tight pores that limit the mass transport, often correspond to a high local flux and hence can be identified within the porous network as red flux lines. The diffusion through the film with lowest porosity, HPC22 in Fig. 1b, was simulated in 5 separate layers where each layer overlapped with the neighboring layers. The uppermost sub-volume is visualised in Fig. 1b. In the film with intermediate porosity, HPC30 in Fig. 1c, two main channels are responsible for the diffusion. This is supported by previous work on HPC30 in the environmental scanning electron microscope that indicated the existence of such localized channels promoting faster water transport (Jansson et al., 2014). The diffusion in the film with highest porosity, HPC45 in Fig. 1f, is evenly distributed throughout the

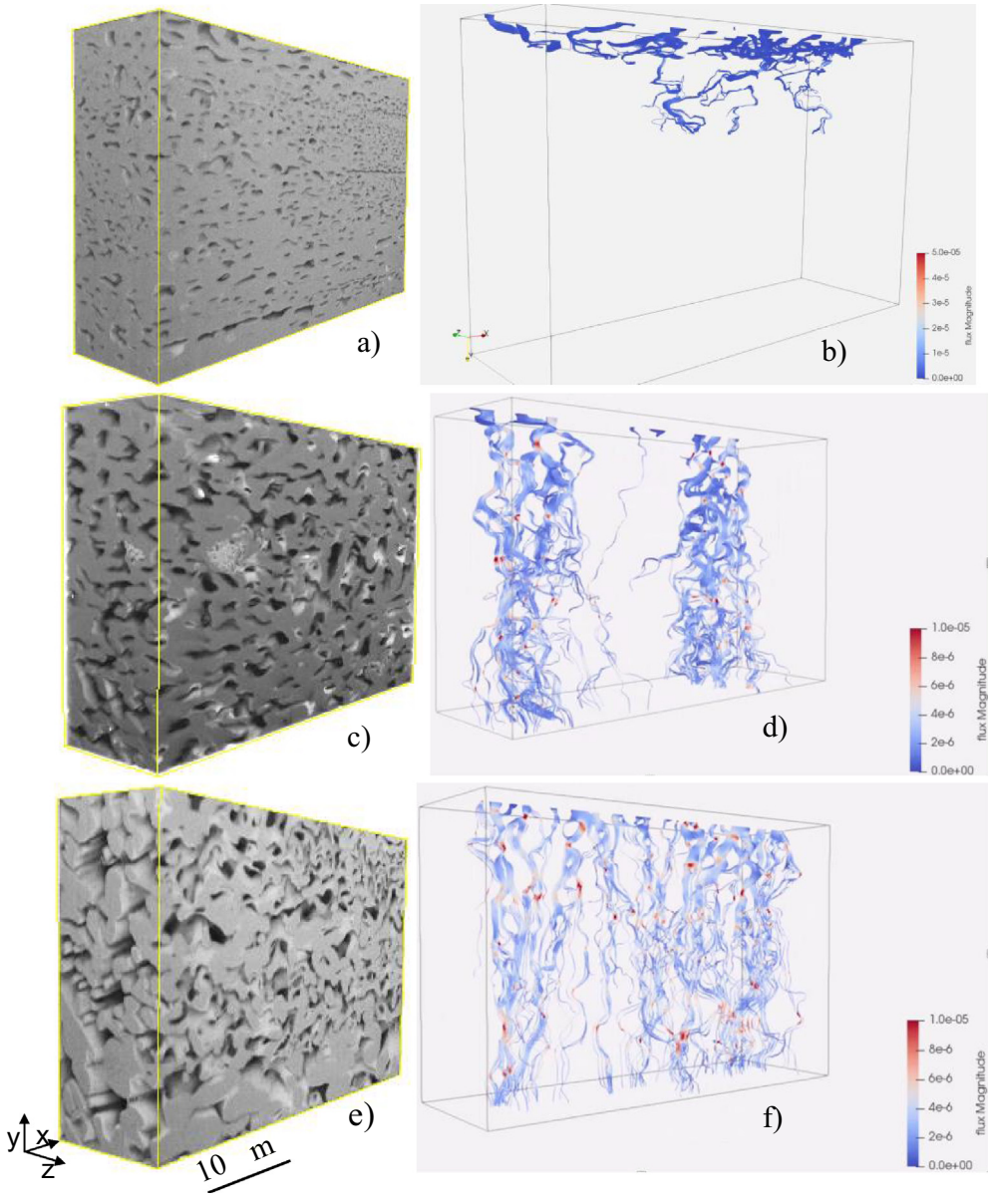

Fig. 1. A 3D reconstruction of leached a) HPC22, c) HPC30 and e) HPC45 obtained using focused ion beam scanning electron microscope tomography and imaged with backscattered electrons. The darker regions correspond to deep pores, the intermediate-intensity regions correspond to the solid ethyl cellulose and the brighter regions correspond to shallow pores. The corresponding 3D simulated diffusion for each film is shown in b) HPC22, d) HPC30 and f) HPC45. The red color corresponds to higher flux values and the blue color to lower flux values. In b), the diffusion is calculated in separate layers due to large internal variation in the porous structure; simulated diffusion in the upper sub-volume is shown. In d) and f), the flux from one single line inlet at the top is shown. For d) HPC30 two main channels can be seen and for f) HPC45 the flux lines are evenly distributed throughout the volume. (For interpretation of the references to color in this figure legend, the reader is referred to the web version of this article.)

porous structure which can be seen by the flux lines being evenly distributed along the line at the upper film surface. However, it should be mentioned that the flux lines can vary depending on where on the upper film surface the starting line for the simulation is taken. It is known from some previous work that there is a percolation onset around 22 wt% of HPC (Marucci et al., 2009). A plausible explanation for HPC45 having a more evenly distributed mass transport through the volume compared to HPC30 and HPC22 is that HPC45 is further away from the percolation onset and thus have the highest porosity and the most well-connected pore structure. The simulated and experimentally measured effective diffusion coefficients are summarized in Table 1.

By comparing the simulated and experimentally measured D_{eff} it can be seen that the simulated data is in all three cases lower than the experimentally measured D_{eff}. The underestimation is in the order of 15–25%. The differences are likely to depend mainly on the fact that only a small part of the film was imaged and used for simulations, while experimental diffusion measurements were made on the entire film, although errors in segmentation and numerical computations may also play a role. Even so, the correspondence between the simulated and experimentally measured D_{eff} is good, especially given that a previous study showed a difference of more than 300% (Wassén et al., 2014). This shows that using the FIB-SEM technology in combination with pore-scale simulations is a successful approach in order to obtain understanding of how the 3D porous structure influences the transport properties.

It is not surprising that the higher the porosity (and HPC content), the larger the value of D_{eff}. Following Barman et al (Barman et al., 2018), we define the *transport ratio*

$$TR = \frac{D_{eff}}{D_0 \phi} \tag{5}$$

which is a measure of all structure properties influencing the effective diffusion except direct scaling with porosity ϕ. The values of TR computed using simulated and measured D_{eff} are shown in Table 1, and show a strong dependence on the HPC content in the film. Note that $TR \leq 1$ always, and that a bundle of straight pores has $TR = 1$. The ratio has often been identified as the inverse of tortuosity squared, $TR = 1/\tau^2$, but as tortuosity has a more precise geometric definition, and there are other features such as connectivity and existence of dead ends which influence D_{eff}, and therefore TR, we prefer not to make this identification. See Barman et al (Barman et al., 2018) for further discussion.

Instead, we aim to determine the influence of the structural parameters geodesic tortuosity τ, see Barman et al (Barman et al., 2018), and constriction factor β, see Holzer et al (Barman et al., 2019). As discussed by Barman et al (Barman et al., 2018), one may hypothesise that

$$TR \approx \frac{\beta}{\tau^2} \tag{6}$$

In Table 2, values for β and τ are shown, computed using the software Mist (Barman et al., 2019). The ratio in eq. (6) is also shown and may be compared to the transport ratio. A comparison shows that eq. (6) is approximately valid for the HPC30 and HPC45 films, with a difference of less than 10%. This suggests that for these films, the most prominent structural properties determining the transport ratio are the tortuous paths and variations in cross-sectional area described by the constriction factor. This is also in line with the analysis of these structures in (Fager et al., 2020), which shows that they are well connected.

The HPC22 film on the other hand has a very low transport ratio and eq. (6) is far from accurate. The tortuosity and constriction factor alone cannot explain the slow diffusion through this film. As was reported by Fager et al (Fager et al., 2020), there are strong bottlenecks in the HPC22 sample, where most of the transport passes through a few narrow channels. The effect of the bottlenecks is not well described by the constriction factor since the variation in pore size is not very large, and only partly described by the tortuosity - which is high, but not high enough to yield the simulated value of TR when inserted into eq. (6). One might consider defining additional structure properties to add to eq. (6) in order to capture the bottleneck effect, but that is beyond the scope of this work.

Simulations of diffusion were also performed for slices of thickness 10 μm at different depth of all the samples. In Fig. 2, the dependence of the effective diffusion coefficient (Fig. 2a) on the depth into the samples is shown together with the corresponding local porosities (Fig. 2b), as well as the local values of the transport ratio (Fig. 2c). The effective diffusion coefficients and porosities vary throughout the depth in all three films, with in general lower porosities towards the bottom of the film. Interestingly, the HPC22 sample is the least homogeneous in terms of D_{eff}, despite relatively modest variations in porosity. By contrast, the HPC30 and HPC45 samples have a fairly strong covariance between D_{eff} and porosity. This is further emphasized by studying the transport ratios in Fig. 2c. It is clear that there are regions in the HPC22 film where higher connectivity and/or lower tortuosity yield a higher transport ratio, while further down into the film the transport ratio decreases due to lower connectivity and bottlenecks. The HPC30 and HPC45 films are more homogeneous with only relatively small variations.

Table 1
A summary of the simulated and experimentally measured effective diffusion coefficients for HPC22, HPC30 and HPC45, which are shown together with the porosities and transport ratios computed using eq. (4). For HPC22, the simulated value of D_{eff} was computed using eq. (3).

HPC [wt %]	Porosity	Simulated D_{eff} [10^{-12} m^2/s]	TR (sim)	Experimental D_{eff} [10^{-12} m^2/s]	TR (exp)
22	0.181	6.10	0.0115	7.52	0.0140
30	0.296	198	0.226	270	0.308
45	0.411	506	0.416	637	0.524

Table 2
The geometric properties geodesic tortuosity and constriction factor for the three films, computed using the software Mist (Barman et al., 2019). The combination β/τ^2, which is expected to correlate well with the transport ratio, is also shown together with the simulated value of TR from Table 1 (repeated for convenience).

HPC [wt %]	Geodesic tortuosity (τ)	Constriction factor (β)	β/τ^2	TR (sim)
22	3.22	0.280	0.0270	0.0115
30	1.24	0.319	0.208	0.226
45	1.12	0.468	0.375	0.416

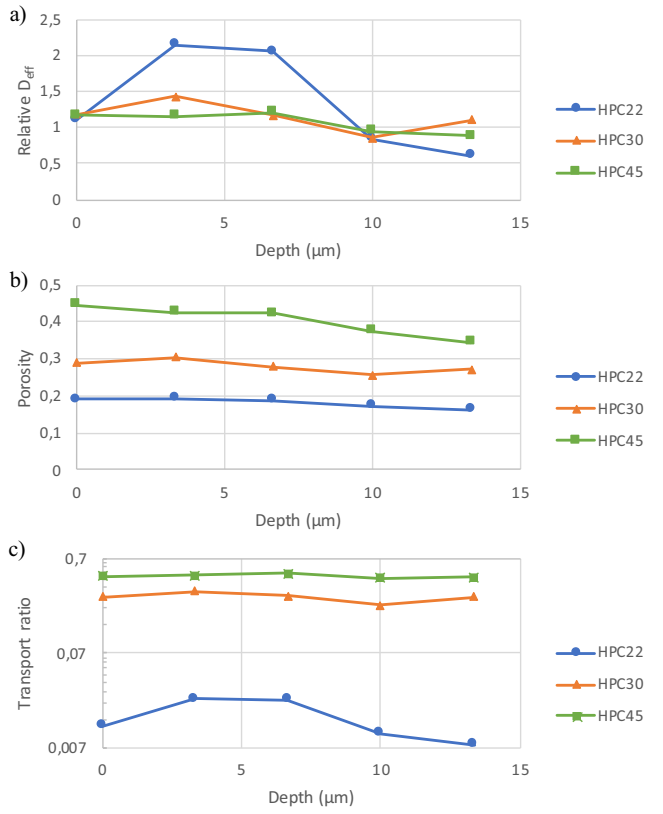

Fig. 2. Local simulated effective diffusion coefficients (relative to the value for the whole structure), porosities and transport ratios computed locally for overlapping slices of thickness 10 μm.

Conclusions

In this work, the detailed 3D structure from FIB-SEM tomography data of porous ethyl cellulose films was used for diffusion simulations. The diffusion simulations were compared with experimentally measured permeability properties. We achieved a good agreement between simulations and experimental data, due to the high-quality 3D structure obtained with the FIB-SEM technique. The results clearly show that with a lower amount of HPC, the pore structure becomes more tortuous and less well connected, leading to lower effective diffusion coefficients than expected if only the porosity would have been considered. Local structural variations and bottlenecks also influence the results strongly.

This work links real experimental 3D structures with simulated and experimental transport properties. The link between the structures and the transport properties is crucial to understand in order to tailor the release properties. This work has provided new valuable insights that facilitate the design of future controlled-release pharmaceuticals with favourable release properties.

CRediT authorship contribution statement

C. Fager: Conceptualization, Methodology, Validation, Formal analysis, Investigation, Writing - original draft, Writing - review & editing, Visualization. **T. Gebäck:** Conceptualization, Methodology, Software, Validation, Formal analysis, Writing - review & editing, Visualization. **J. Hjärtstam:** Methodology, Validation, Formal analysis, Investigation, Writing - original draft. **M. Röding:** Methodology, Software, Validation, Data curation, Writing - review & editing, Visualization. **A. Olsson:** Validation, Investigation, Resources, Writing - review & editing, Supervision. **N. Lorén:** Validation, Investigation, Resources, Writing - review & editing, Supervision, Project administration. **C. Corswant:** Validation, Investigation, Resources, Writing - review & editing, Supervision, Project administration. **A. Särkkä:** Conceptualization, Methodology, Formal analysis, Writing - review & editing, Supervision. **E. Olsson:** Conceptualization, Methodology, Validation, Investigation, Writing - review & editing, Supervision, Project administration, Funding acquisition.

Declaration of Competing Interest

The authors declare that they have no known competing financial interests or personal relationships that could have appeared to influence the work reported in this paper.

Acknowledgment

The authors would like to gratefully acknowledge the Swedish Foundation for Strategic Research (SSF grant AM13-412 0066) project "Material structures seen through microscopes and statistics" for funding this work, AstraZeneca for providing the material and Chalmers Material Analysis Laboratory for their support of microscopes. Furthermore, we gratefully acknowledge Sandra Barman for valuable discussions.

References

Armatas, G.S., 2006. Determination of the effects of the pore size distribution and pore connectivity on the pore tortuosity and diffusive transport in model porous networks. Chem. Eng. Sci. 61, 4662–4675.

Barman, S,, Bolin, D., Fager, C., Gebäck, T., Lorén, N., Olsson, E., Särkkä, A., 2019. Mist- a program package for visualization and characterization of 3D geometries, https://mist.math.chalmers.se.

Barman, S., Rootzen, H., Bolin, D., 2018. Prediction of diffusive transport through polymer films from characteristics of the pore geometry. AIChE J. 65 (1), 446–457. https://doi.org/10.1002/aic.16391.

Blomqvist, C., 2016. Nano-particulate silica hydrogels imaged in 2D and 3D using TEM: Effects of local pore structure on mass transport and applications in aggregation dynamics. PhD Thesis. 2016. DOI: https://research.chalmers.se/publication/246500.

Fager, C., Barman, S., Röding, M., Olsson, A., Lorén, N., von Corswant, C., Bolin, D., Rootzén, H., Olsson, E., 2020. 3D high spatial resolution visualisation and quantification of interconnectivity in polymer films. Int. J. Pharm. 587, 119622. https://doi.org/10.1016/j.ijpharm.2020.119622.

Fager, C., Röding, M., Olsson, A., Lorén, N., Von Corswant, C., Särkkä, A., Olsson, E., 2020. Optimisation of FIB-SEM tomography and reconstruction for soft, porous and poorly conducting materials. Microscopy and Microanalysis. 26(4), 837–845. DOI: https://doi.org/10.1017/S1431927620001592.

Gårdebjer, S., Larsson, M., Gebäck, T., Skepö, M., Larsson, A., 2018. An overview of the transport of liquid molecules through structured polymer films, barriers and composites – experiments correlated to structure-based simulations. Adv. Coll. Interface Sci. 256, 48–64. https://doi.org/10.1016/j.cis.2018.05.004.

Gebäck, T., Heintz, A., 2014. A lattice Boltzmann method for the advection-diffusion equation with neumann boundary conditions. Commun. Computat. Phys. 15 (2), 487–505.

Gebäck, T., Marucci, M., Boissier, C., Arnehed, J., Heintz, A., 2015. Investigation of the effect of the tortuous pore structure on water diffusion through a polymer film using lattice Boltzmann simulations. J. Phys. Chem. B 119, 5220–5227.

Ghassemzadeh, J., Sahimi, M., 2004. Pore network simulation of fluid imbibition into paper during film: II. Characterization of paper's morphology and computation of its effective permeability tensor. Chem. Eng. Sci. 59, 2265–2280.

Giannuzzi, L.A., Stevie, F.A., 2005. Introduction to focused ion beams: Instrumentation, theory, techniques and practise. Springer, USA.

Ginzburg, I., 2005. Equilibrium-type and link-type lattice boltzmann models for generic advection and anisotropic-dispersion equation. Adv. Water Resour. 28, 1171–1195.

Holzer, D., Wiedenmann B., Münch L., Keller M., Prestat Ph., Gasser, I., Robertson, B., 2013. Grobéty. The influence of constrictivity on the effective transport properties of porous layers in electrolysis and fuel cells. Mater Sci. 48, 2934–2952.

Jansson, A., Boissier, C., Marucci, M., Nicholas., Gustafsson, S., Hermansson, A.-M., Olsson, 2014. Novel method for visualizing water transport through phase-separated polymer films. Microscopy Microanal. 20, 394–406.

Jones, A.C., Arns, C.H., Hutmacher, D.W., Milthorpe, B.K., Sheppard, A., M.A., 2009. The correlation of pore morphology, interconnectivity and physical properties of 3D ceramic scaffolds with bone ingrowth. Biomaterials 30, 1440–1451.

Krüger, T., Kusumaatmaja, H., Kuzmin, A., Shardt, O., Silva, G., Viggen, E.M., 2017. The Lattice Boltzmann method. Springer International Publishing; 2017. (DOI: 10.1007/978-3-319-44649-3).

Lindstedt, B., Ragnarsson, G., Hjärtstam, J., 1989. Osmotic pumping as a release mechanism for membrane-coated drug formulations. Int. J. Pharm. 56, 261–268.

Markl, D., Wang, P., Ridgway, C., Karttunen, A-P., Bawuah, P., Ketolainen, J., Gane, P., Peiponen, K-E., Zeitler, A., 2018. Resolving the rapid water absorption of porous functionalised calcium carbonate powder compacts by terahertz pulsed imaging. Chem. Eng. Res. Des. 132, 1082–1090.

Marucci, M., Hjärtstam, J., Ragnarsson, G., Iselau, F., Axelsson, A., 2009. Coated formulations: new insights into the release mechanism and changes in the film properties with a novel release cell. J. Control. Release 136 (3), 206–212.

Mathworks, Natick, MA, US.

Mayer, Joachim, Giannuzzi, Lucille A., Kamino, Takeo, Michael, Joseph, 2007. TEM Sample Preparation and FIB-Induced Damage. MRS Bull. 32 (5), 400–407.

Mills, R., 1973. Self-diffusion in normal and heavy water in the range 1–45°. J. Phys. Chem. 77 (5), 685–688. https://doi.org/10.1021/j100624a025.

Narayan, Kedar, Subramaniam, Sriram, 2015. Focused ion beams in biology. Nat. Methods 12 (11), 1021–1031.

Röding, M., Schuster, E., Logg, K., Lundman, M., Bergström, P., Hanson, C., Gebäck, T., Lorén, N., 2016. Computational high-throughput screening of fluid permeability in heterogeneous fiber materials. Soft Matter 12, 6293–6299.

Röding, M., Fager, C., Olsson, A., Von Corswant, C., Olsson, E., Lorén, N., 2021. Three-dimensional reconstruction of porous polymer films from FIB-SEM nanotomography data using random forests. J. Microsc. 281 (1), 76–86. https://doi.org/10.1111/jmi.v281.110.1111/jmi.12950.

Schneider, Caroline A, Rasband, Wayne S, Eliceiri, Kevin W, 2012. NIH Image to ImageJ: 25 years of image analysis. Nat. Methods 9 (7), 671–675.

Siepmann, F., Hoffmann, A., Leclercq, B., Carling, B., Siepmann, J., 2007. How to adjust desired drug release patterns from ethylcellulose-coated dosage forms. J. Control. Release 119, 182–189.

Stenzel, O., Pecho, O., Holzer, L., 2016. Predicting effective conductivities based on geometric structure characteristics. AIChE J. 62 (5), 1834–1843.

Vogel, H.J., 1997. Morphological determination of pore connectivity as a function of pore size using serial sections. Eur. J. Soil Sci. 48, 365–377.

Wassén, S., Bordes, R., Gebäck, T., Bernin, D., Schuster, E., Lorén, N., Hermansson, A.-M., 2014. Probe diffusion in phase-separated bicontinuous biopolymer gels. Soft Matter. https://doi.org/10.1039/c4sm01513.

Yang, B.H., Wu, A.-X., Miao, X., Liu, J.-Z., 2014. 3D characterization and analysis of pore structure of packed ore particle beds based in computed tomography images. Trans. Nonferrous Met. Soc. 24, 833–838.